J. Astrophys. Astr. (2022)43:31
https://doi.org/10.1007/s12036-022-09815-w

MISCELLANEOUS

Optical observations of star clusters NGC 1513 and NGC 4147; white dwarf WD 1145+017 and *K* band imaging of star-forming region Sh 2-61 with the 3.6-m Devasthal optical telescope

RAM SAGAR[1,2], R. K. S. YADAV[2,*], S. B. PANDEY[2], SAURABH SHARMA[2], SNEH LATA[2] and SANTOSH JOSHI[2]

[1]Indian Institute of Astrophysics, Sarajapur Road, Koramangala, Bengaluru 560034, India.
[2]Aryabhatta Research Institute of Observational Sciences, Manora Peak, Nainital 263001, India.
Corresponding author. E-mail: rkant@aries.res.in

MS received 16 November 2021; accepted 13 January 2022

Abstract. The *UBVRI* CCD photometric data of open star cluster NGC 1513 are obtained with the 3.6-m Indo-Belgian Devasthal optical telescope (DOT). Analyses of the GAIA EDR3 astrometric data have identified 106 possible cluster members. The mean proper motion of the cluster is estimated as $\mu_\alpha \cos\delta = 1.29 \pm 0.02$ and $\mu_\delta = -3.74 \pm 0.02$ mas yr^{-1}. Estimated values of reddening $E(B-V)$ and distance to the NGC 1513 are 0.65 ± 0.03 mag and 1.33 ± 0.1 kpc, respectively. Age of 225 ± 25 Myr is assigned to the cluster by comparing theoretical isochrones with deeply observed cluster sequences. Using observations taken with the 3.6-m DOT, values of distance and age of the galactic globular cluster NGC 4147 are estimated as 18.2 ± 0.2 Kpc and 14 ± 2 Gyr, respectively. The optical observations of planetary transit around white dwarf WD 1145+017 and *K*-band imaging of star-forming region Sharpless Sh 2-61 demonstrate observing capability of 3.6-m DOT. Optical and near-infrared observations of celestial objects and events are being carried out routinely with the 3.6-m DOT. They indicate that the performance of the telescope is at par with those of other similar telescopes located elsewhere in the world. We, therefore, state that this observing facility augurs well for multi-wavelength astronomy including the study of astrophysical jets.

Keywords. Star clusters—NGC 1513—NGC 4147—WD 1145+017—Sh 2-61—CCD imager.

1. Introduction

The 3.6-m Indo-Belgian Devasthal optical telescope (DOT) is located at the mountain peak (longitude = 79°.7 E, latitude = 29°.4 N, altitude = 2424 ± 4 m) of Devasthal (meaning 'abode of God') in Nainital district of Kumaun region, Uttarakhand. The location was identified after decades of detailed site survey using modern instruments (Sagar *et al.* 2000; Stalin *et al.* 2001 and references therein). The telescope and its performance are described in details by Kumar *et al.* (2018), Omar *et al.* (2017) and Sagar *et al.* (2019a,b, 2020).

Being a joint venture between India and Belgium, the 3.6-m DOT was technically activated jointly by premiers of both countries from Brussels, Belgium on 30 March 2016. Since then, the telescope is used routinely for carrying out optical and near-infrared (NIR) observations of galactic and extra-galactic celestial objects as well as transient astronomical events (Pandey 2016; Gupta *et al.* 2021a,b; Kumar *et al.* 2021a,b; Pandey *et al.* 2021). Presently, there are 4 back-end instruments at the 3.6-m DOT. Two of them namely 4K×4K CCD imager (Pandey *et al.* 2018; Kumar *et al.* 2021c) and ARIES Devasthal faint object spectrograph Camera (ADFOSC) (Omar *et al.* 2019a,b,c) are used for optical observations while TIFR Near

This article is part of the Special Issue on "Astrophysical Jets and Observational Facilities: A National Perspective".

Published online: 28 May 2022

Table 1. Existing relevant studies of NGC 1513 are listed in chronological order.

Study	Pass bands	Radius (arc-min)	Distance (parsec)	$E(B-V)$ (mag)	log(t)	Lm (mag)	Reference
PG, PM	m_{pg}					$m_{pg} \sim 14$	1
PG photometry	m_{pg}, m_V	7	860			$m_{pg} \sim 16.5$	2
PE, PG photometry	*UBV*, *RGU*	7	1320	0.53	8.18	$G \sim 16.5$	3
PM, CCD photometry	*BV*		1320	0.67	8.4	$V \sim 16.5$	4
CCD photometry	*BV*	9.2	1320	0.76	7.4	$V \sim 19$	5

In the first column, studies based on photographic, proper motion, photoelectric and charge-coupled devices are abbreviated as PG, PM, PE and CCD, respectively. Letter t in column 6 denotes age (in years). Limiting magnitude of the study is denoted by Lm in column 7. In column 8, 1: Bronnikova (1958); 2: Barkhatova & Dryakhlushina (1960); 3: del Rio & Huestamendia (1988); 4: Frolov *et al.* (2002) and 5: Maciejewski & Niedzielski (2007).

Infrared Imaging Camera-II (TIRCAM2) and TIFR-ARIES Near Infrared Spectrometer (TANSPEC) are used for NIR observations (Ojha *et al.* 2018; Baug *et al.* 2018). Both optical and NIR observations taken with these instruments have shown that angular resolutions and detection limits achieved with the telescope are at par with similar telescopes located elsewhere in the globe (Sagar *et al.* 2019a,b, 2020 and references therein).

In this paper, we present CCD optical broad band photometric and *K* band observations taken with the 3.6-m DOT. Star cluster NGC 1513 and NGC 4147 and white dwarf WD 145+07 were observed using CCD imager while TIRCAM2 was used for *K* band imaging of star-forming region Sh 2-61. These observations and multi-wavelength archival data are used to derive precise astrophysical parameters of the star clusters under study. The outline of the paper is as follows. Sections 2 to 5 are devoted to the open star cluster NGC 1513. The optical observations of cluster NGC 4147; planetary transits around WD 1145+017 and deep *K*-band imaging of a star-forming region Sharpless Sh 2-61 are discussed in Sections 6, 7 and 8, respectively. The summary and conclusions are presented in the last section.

2. Open star cluster NGC 1513

The member stars in open star clusters are loosely concentrated and gravitationally bound to each other. The GAIA EDR3 kinematical data are very important to interrogate the motion of open star clusters. The proper motion and parallax data are being frequently used to identify the cluster members as they play a very crucial role in deriving the basic parameters of the clusters (Yadav *et al.* 2008, 2013).

The open cluster NGC 1513 is located in the Perseus arm of the Milky Way. Its equatorial and galactic coordinates are $\alpha_{2000} = 04^{h}09^{m}98^{s}$, $\delta_{2000} = 49°31'00''$ and $l = 152°.6$, $b = -1°.57$, respectively. This cluster is classified as II2m, a moderately rich cluster with little central concentration by Trumpler (1930). Bronnikova (1958) determined the proper motion and membership probability using photographic plates having an epoch difference of $\sim$55 years. Radius of the cluster is estimated to be $\sim 7'$ (see Table 1). Barkhatova & Dryakhlushina (1960) and del Rio & Huestamendia (1988) investigated the cluster by carrying out photographic and photoelectric photometry of 49 and 116 stars, respectively. Frolov *et al.* (2002) studied this cluster astrometrically and identified 33 probable members of the cluster. Using CCD *BV* data, cluster parameters have been determined by Maciejewski & Niedzielski (2007). All these information are tabulated in Table 1. They indicate that cluster age is $\sim$100 Myr while distance is $\sim$1.3 Kpc.

As evident from the above literature surveys and Table 1, NGC 1513 lacks multi-wavelength deep *UBVRI* CCD photometric study. Also, existing studies are mainly limited to $V \sim 16$ mag and hampered by field star contamination. Detailed photometric and kinematical studies of this poorly studied intermediate-age star cluster NGC 1513 are carried out below by combining present *UBVRI* CCD photometric data with the GAIA EDR3 high precision proper motion data.

2.1 *Observations and data reductions*

NGC 1513 was observed in *UBVRI* photometric passband on 2 and 3 November 2016 with the 3.6-m

Table 2. Log of optical observations of NGC 1513 are given along with exposure times in each filter.

	Exposure time (in s) in filter				
Date	*U*	*B*	*V*	*R*	*I*
2 November 2016	300 × 2	300 × 6	300 × 2	300 × 6	10 × 2
3 November 2016	30 × 2	30 × 2	10 × 2	10 × 3	–

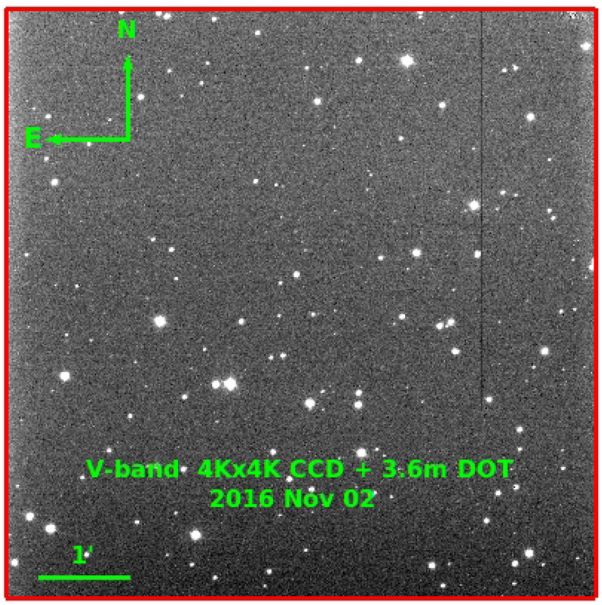

Figure 1. *V* image of the cluster NGC 1513 taken with 3.6-m DOT. North is up and East is left.

DOT. Images were collected with 4K×4K CCD camera in 4×4 binning mode. At the $f/9$ Cassegrain focus of the telescope, a 15 μm pixel size of the CCD camera covers $0''.1$ on the sky and field-of-view of the camera becomes $6'.5 \times 6'.5$. The gain and readout noise of CCD is 5 e^{-1}/ADU and 10 e^{-1} (Pandey *et al.* 2018), respectively. Log of observations is listed in Table 2. Figure 1 shows the observed cluster image in *V* filter. We adopted the standard procedure for raw-data processing in the IRAF[1] environment. The DAOPHOT/ALLSTAR (Stetson 1987, 1992) software was used to do the photometry. The photometry was done on individual images. The instrumental magnitudes were derived using quadratically varying point spread function (PSF). The magnitudes were aligned to that of the deepest frame for each filter and the final catalog was created including all the objects identified at least in two filters.

The Landolt standard field PG0231 (Landolt 1992) was observed to transfer the instrumental magnitudes into standard values. For this, we used six standard stars. Their range in brightness and colors are $12.77 \leq V \leq 16.10$ and $-0.34 < (B-V) < 1.44$, respectively. The transformation equations obtained are as follows:

$$u = U + 3.50 \pm 0.01 - (0.09 \pm 0.01)(U-B) + (0.49 \pm 0.02)X,$$

$$b = B + 1.66 \pm 0.01 - (0.09 \pm 0.01)(B-V) + (0.32 \pm 0.01)X,$$

$$v = V + 1.58 \pm 0.01 + (0.04 \pm 0.01)(B-V) + (0.21 \pm 0.01)X,$$

$$r = R + 1.51 \pm 0.01 + (0.09 \pm 0.01)(V-R) + (0.13 \pm 0.01)X,$$

$$i = I + 1.72 \pm 0.01 - (0.04 \pm 0.02)(V-I) + (0.08 \pm 0.01)X,$$

where u, b, v, r and i are the aperture corrected instrumental magnitudes and U, B, V, R and I are standard magnitudes whereas X is the air mass. For the atmospheric extinction coefficients, we assumed the typical values for the Devasthal site (Pandey *et al.* 2018). The errors in zero points and color coefficients are ~ 0.01 mag. The X and Y coordinates of the stars in the observed region are converted to right ascension (RA) and Declination (Dec) of J2000. To get the astrometric solution, we used the SkyCat tool and guide star catalog v2 (GSC-2). We considered 100 bright stars for which we have both RA and Dec and the corresponding pixel coordinates. By using the task CCMAP and CCTRAN under IRAF, we converted the pixel coordinates into RA and Dec of all the stars observed in the field. The U, B, V, R and I magnitudes of all stars observed in the region of NGC 1513 are listed in Table 3 along with RA, Dec and proper motion membership probability. A sample of this table is given here, while the full table is available online as well as from the corresponding author.

[1]IRAF is distributed by the National Optical Astronomical Observatory which is operated by the Association of Universities for Research in Astronomy, under contract with the National Science Foundation.

Table 3. A sample table of the catalog for the open cluster NGC 1513.

ID	X (pixel)	Y (pixel)	RA J2000	Dec J2000	U (mag)	eU (mag)	B (mag)	eB (mag)	V (mag)	eV (mag)	R (mag)	eR (mag)	I (mag)	eI (mag)	MP
1	531.257	18.157	4:10:07.96	49:33:54.1	16.031	0.053	15.394	0.020	14.600	0.027	14.113	0.005	13.604	0.003	72
2	597.253	18.176	4:10:06.66	49:33:54.2	99.999	9.999	99.999	9.999	21.765	9.999	20.308	9.999	19.189	9.999	0
3	6.203	26.257	4:10:18.27	49:33:51.7	20.859	9.999	22.205	9.999	99.999	9.999	99.999	9.999	99.999	9.999	0
4	4.954	28.463	4:10:18.30	49:33:51.3	99.999	9.999	20.844	1.110	18.971	0.110	99.999	9.999	99.999	9.999	0
5	1441.349	30.289	4:09:50.08	49:33:53.0	20.072	0.093	18.779	0.013	17.036	0.003	16.021	0.007	15.028	0.017	0
–	–	–	–	–	–	–	–	–	–	–	–	–	–	–	–
–	–	–	–	–	–	–	–	–	–	–	–	–	–	–	–

The full table is available electronically. The (X, Y) pixel positions, RA and Dec sky coordinates and U, B, V, R and I CCD magnitudes with corresponding DAOPHOT errors are listed in columns 2 to 15 while GAIA EDR3 proper motion membership probability (MP) is given in the last column.

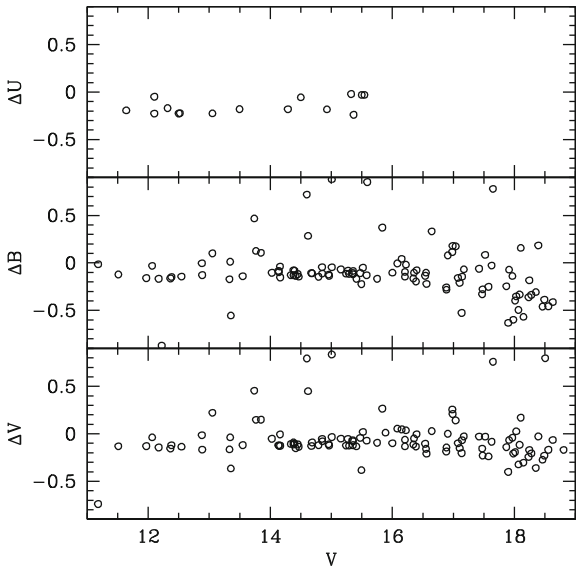

Figure 2. Comparison of photometric U, B and V magnitudes. B and V CCD magnitudes are taken from Maciejewski & Niedzielski (2007) while photoelectric U magnitudes are taken from del Rio & Huestamendia (1988). The difference in magnitudes (ΔU, ΔB and ΔV) are the present minus literature values.

Figure 2 shows the comparison of the present photometry with B and V CCD data from Maciejewski & Niedzielski (2007) and photoelectric U data from del Rio & Huestamendia (1988). We have cross-identified the photometric catalogs by assuming that stars are correctly matched if the difference in position is < 1 arc-sec. In this way, we identified 103 common stars in B and V and only 13 stars in U. The mean values of the difference between two photometries are -0.07 ± 0.06, -0.07 ± 0.08 and -0.14 ± 0.08 mag in V, B and U filters, respectively. This indicates that present magnitudes are in fair agreement with literature except for U mag where the difference is large.

The left panel of Figure 3 shows the internal errors in U, B, V, R and I magnitudes derived from DAOPHOT against V magnitude. The mean errors are ≤ 0.03 mag at $V \sim 20$th mag for B, V, R and I magnitudes while they are ≤ 0.04 mag for U magnitude at $V \sim 18$th mag.

3. Proper motion data of NGC 1513

The kinematical data of clusters are very useful for separating cluster members from field stars and also for estimating the mean proper motion of the cluster. We,

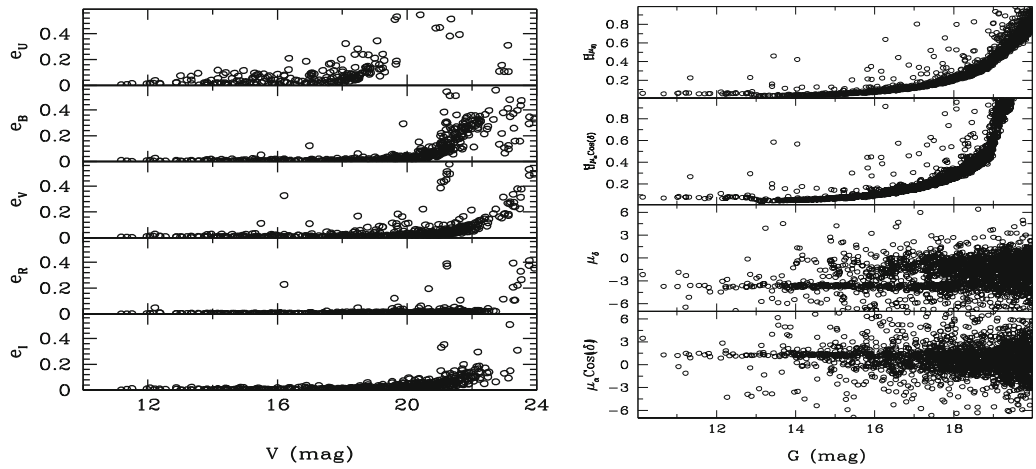

Figure 3. Left panel: DAOPHOT errors in U, B, V, R and I band against V magnitude. Right panel: GAIA EDR 3 catalog proper motion $\mu_\alpha \cos\delta$ and μ_δ with their errors against G mag.

therefore, downloaded the kinematical data from the GAIA EDR3 catalog (Gaia Collaboration *et al.* 2018) within the radius of $\sim 10'$ around the center of NGC 1513. It provides positions on the sky (α, δ), parallaxes and proper motions $(\mu_\alpha \cos\delta, \mu_\delta)$ with limiting magnitude of $G = 21$ mag. The error in parallax is ~ 0.04 milli-arc-second (mas) for stars brighter than $G \sim 15$ mag while for stars of $G \sim 17$ mag, it is ~ 0.1 mas. The proper motions and their corresponding errors for the cluster NGC 1513 are plotted against G magnitude in the right panel of Figure 3. The errors in the corresponding proper motion components are ~ 0.05 mas yr^{-1} for $G \leq 15$ mag), ~ 0.2 mas yr^{-1} for $G \sim 17$ mag and ~ 1.2 mas yr^{-1} for $G \sim 20$ mag.

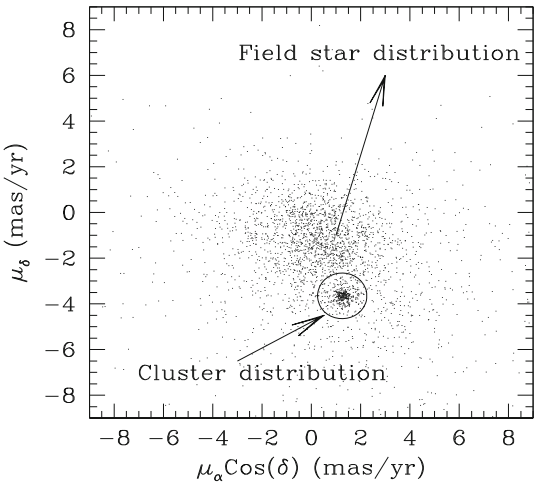

Figure 4. Proper motion vector-point diagram (VPD) of the stars in the region NGC 1513. The distributions of cluster members and field stars are shown with arrows. Both distributions are visible in the VPD.

3.1 *Mean proper motion*

In Figure 4, we show the vector-point diagram (VPD) of stars located in the region of NGC 1513 using the proper motion data in right accession $(\mu_\alpha \cos\delta)$ and declination (μ_δ) directions. An inspection of the VPD exhibits two groups of stars. The dense population of stars shows the cluster members' distribution while the scattered distribution represents the field stars. To select the probable cluster members, only stars located within a circle of 1 mas yr^{-1} radius shown in Figure 4 are considered. The radius of the circle is chosen as the best compromise between losing members with poor proper motions, and including field stars.

To estimate the mean proper motion of the cluster, we plot histograms of the above-selected cluster members in both $\mu_\alpha \cos\delta$ and μ_δ directions in Figure 5. The fitting of Gaussian function to the histograms, provides the

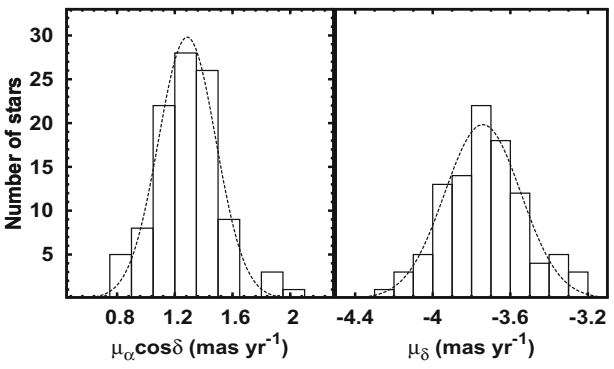

Figure 5. The proper motion histogram in $\mu_\alpha \cos\delta$ and μ_δ in a bin of 0.1 mas yr^{-1}. The Gaussian function is fitted to the histograms to the central bins.

mean proper motions as 1.286 ± 0.015 and -3.742 ± 0.016 mas yr^{-1} in $\mu_\alpha \cos\delta$ and μ_δ, respectively. These precise estimates agree very well with the corresponding values of 1.324 ± 0.177 and -3.679 ± 0.161, respectively, derived by Cantat-Gaudin *et al.* (2018) for this cluster.

3.2 *Proper motion membership probability*

The cluster membership probability of a star is determined following the method described by Balaguer-Nunez *et al.* (1998). For this, first proper motion frequency distributions of cluster stars (ϕ_c^v) and field stars (ϕ_f^v) are constructed by the equations given below:

$$\phi_c^v = \frac{1}{2\pi\sqrt{(\sigma_c^2+\epsilon_{xi}^2)(\sigma_c^2+\epsilon_{yi}^2)}} \times \exp\left\{-\frac{1}{2}\left[\frac{(\mu_{xi}-\mu_{xc})^2}{\sigma_c^2+\epsilon_{xi}^2}+\frac{(\mu_{yi}-\mu_{yc})^2}{\sigma_c^2+\epsilon_{yi}^2}\right]\right\}$$

and

$$\phi_f^v = \frac{1}{2\pi\sqrt{(1-\gamma^2)}\sqrt{(\sigma_{xf}^2+\epsilon_{xi}^2)(\sigma_{yf}^2+\epsilon_{yi}^2)}} \times \exp\left\{-\frac{1}{2(1-\gamma^2)}\left[\frac{(\mu_{xi}-\mu_{xf})^2}{\sigma_{xf}^2+\epsilon_{xi}^2}.\right.\right. \left.\left. -\frac{2\gamma(\mu_{xi}-\mu_{xf})(\mu_{yi}-\mu_{yf})}{\sqrt{(\sigma_{xf}^2+\epsilon_{xi}^2)(\sigma_{yf}^2+\epsilon_{yi}^2)}}+\frac{(\mu_{yi}-\mu_{yf})^2}{\sigma_{yf}^2+\epsilon_{yi}^2}\right]\right\},$$

where (μ_{xi}, μ_{yi}) are the proper motions of ith star, while $(\epsilon_{xi}, \epsilon_{yi})$ are the corresponding proper motion errors. (μ_{xc}, μ_{yc}) and (μ_{xf}, μ_{yf}) represent the center of the cluster and field proper motion distributions, respectively. For the cluster members, the intrinsic proper motion dispersion is denoted by σ_c, whereas σ_{xf} and σ_{yf} exhibit the field intrinsic proper motion dispersion. The correlation coefficient γ is calculated as:

$$\gamma = \frac{(\mu_{xi}-\mu_{xf})(\mu_{yi}-\mu_{yf})}{\sigma_{xf}\sigma_{yf}}.$$

To calculate ϕ_c^v and ϕ_f^v, we considered those stars which have proper motion errors ≤ 1 mas yr^{-1}. The center of the cluster proper motion is considered as mean proper motion derived in previous section. The intrinsic proper motion dispersion for the cluster stars (σ_c) could not be determined reliably using the present proper motion data. Assuming a distance of 1.33 kpc derived in the next section, and radial velocity dispersion 1 km s^{-1} for open clusters (Girad *et al.* 1989), the expected dispersion in proper motion would be ~ 0.15 mas yr^{-1}. For field stars, we have $(\mu_{xf}, \mu_{yf}) = (0.5, -1.3)$ mas yr^{-1} and $(\sigma_{xf}, \sigma_{yf}) = (1.7, 1.6)$ mas yr^{-1}. The n_c and n_f are the normalized number of cluster and field stars, respectively, (i.e., $n_c + n_f = 1$), the total distribution function can be calculated as:

$$\phi = (n_c \times \phi_c^v) + (n_f \times \phi_f^v).$$

Now, the membership probability (MP) for the ith star is derived as:

$$P_\mu(i) = \frac{\phi_c(i)}{\phi(i)}.$$

The value of MP for each star is listed in Table 3 along with photometric and other relevant data.

Earlier, Frolov *et al.* (2002) determined the proper motion of stars using the photographic plates. They considered the stars with proper motion error ≤ 2 mas yr^{-1} for membership determination. There are 92 stars common between us and Frolov *et al.* (2002). We found 42 stars in Frolov *et al.* (2002) and 33 stars in our study which have an MP $> 50\%$. Because of the better accuracy of proper motion data in GAIA EDR3 (≤ 1 mas yr^{-1}), the present estimate of MP is more reliable than the previous study. Out of 554 stars observed in the region of NGC 1513, only 106 stars have MP $\geq 50\%$. All these stars have been considered as cluster member and are used for estimating cluster parameters in the following sections.

4. Parameters of the cluster NGC 1513

4.1 *Reddening*

To estimate the reddening towards the cluster region, we plot $(U-B)$ *vs* $(B-V)$ color–color diagram of the stars having membership probability more than 50% in Figure 6. The intrinsic ZAMS given by Schmidt-Kaler (1982) is fitted by considering the slope of reddening line as $E(U-B)/E(B-V) = 0.72$. Visual fitting of ZAMS to the color–color diagram provides a reddening value of $E(B-V) = 0.65 \pm 0.03$ mag for the NGC 1513. The present estimate of reddening is very close to the corresponding value of 0.67 mag estimated by del Rio & Huestamendia (1988).

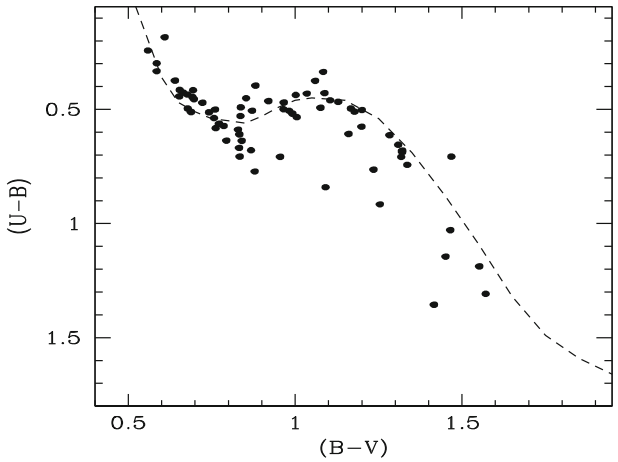

Figure 6. The $(U-B)$ *vs* $(B-V)$ color–color diagram using the cluster members. The dotted line represents the locus of Schmidt-Kaler (1982) ZAMS overplotted on the observed stars.

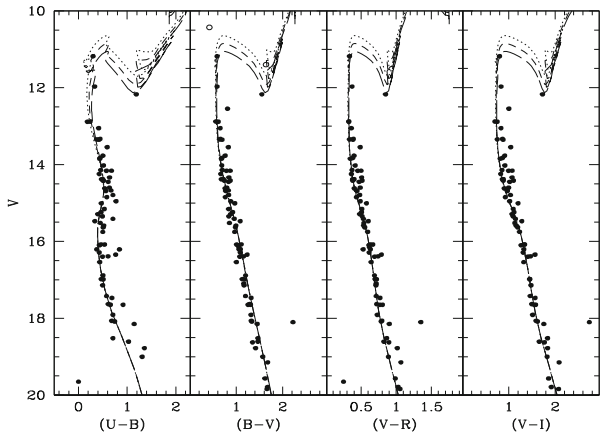

Figure 7. The V *vs* $(U-B)$, V *vs* $(B-V)$, V *vs* $(V-R)$, and V *vs* $(V-I)$ color-magnitude diagrams of the cluster based on the stars having MP $> 50\%$. The over plotted dotted, short dash and long dash lines are the isochrones of log(age) 8.30, 8.35 and 8.40 with $z = 0.019$ taken from Girardi *et al.* (2000).

4.2 *Age and distance*

The photometric color-magnitude diagrams (CMD) are used to estimate the age and distance of the cluster. The detailed shape and different features in the CMDs mainly depend on the age and metallicity of the cluster. The CMDs of GAIA EDR3 proper motion cluster members are shown in Figure 7. It is the deepest V, $(U-B)$; V, $(B-V)$; V, $(V-R)$ and V, $(V-I)$ CMDs extending up to $V \sim 21$ mag except in V, $(U-B)$ CMD where it is only up to $V \sim 19$ mag. A well-defined cluster main-sequence is visible in all the CMDs. Two bright stars, identified as proper motion cluster members by Frolov *et al.* (2002), but could not be observed by us, are also plotted in Figure 7. One giant star has been saturated while the blue straggler is outside from our observed field of view. Their photometric data are borrowed from Frolov *et al.* (2002) and WEBDA catalog of open star clusters. One of them is a red giant in the helium-burning stage of stellar evolution while another one is the possible blue straggler star. Another red giant, observed by us, is also a proper motion cluster member.

The age of the cluster is determined by fitting the theoretical stellar evolutionary isochrones of $Z = 0.019$ taken from Girardi *et al.* (2000). The isochrones of log(age) $= 8.30$, 8.35 and 8.40 are over plotted with dotted, short dash and long dash lines in all the CMDs. The overall visual fits of isochrones in the CMDs are satisfactory. The detailed shape of the main sequence and turn-off are reproduced. The best fitting isochrone to the main-sequence and turn-off provides an age of the cluster as 225 ± 25 Myr $(\log(t) = 8.35)$. The present age estimate is in good agreement with $\log(t) = 8.4$ derived by Frolov *et al.* (2002). The inferred apparent distance modulus $(m-M) = 12.60 \pm 0.15$ mag provides a heliocentric distance as 1.33 ± 0.10 kpc which is very close to the value of 1.32 Kpc derived by del Rio & Huestamendia (1988).

5. Luminosity and mass function of NGC 1513

For reliable estimation of luminosity and mass function of a star cluster, the first necessary step is to remove the field star contamination from the sample of stars. This has been done using proper motion MP derived in Section 3.2. Only stars with MP $\geq 50\%$ are considered as cluster members. In order to avoid errors introduced due to data incompleteness, We have considered stars $V \leq 19$ mag only. The completeness is $\sim 100\%$ at the level of 19th mag (Fabricius *et al.* 2021).

To construct the luminosity function (LF), $V/(V-I)$ color-magnitude has been used and the apparent V magnitude is converted into the absolute magnitude (M_v) using the distance modulus of the cluster. The histogram of brightness distribution, i.e., LF is shown in Figure 8. The LF of the cluster rises until $M_v = 1.5$ mag and then decreases. Based on the cluster parameters derived in this study and theoretical models given by Girardi *et al.* (2000), we have converted LF into the mass function (MF) as shown in Figure 9. The MF slope is estimated using the relation $\log dN/dM = -(1+x)\log(M) +$ constant. Here, dN represents the number of stars in a mass

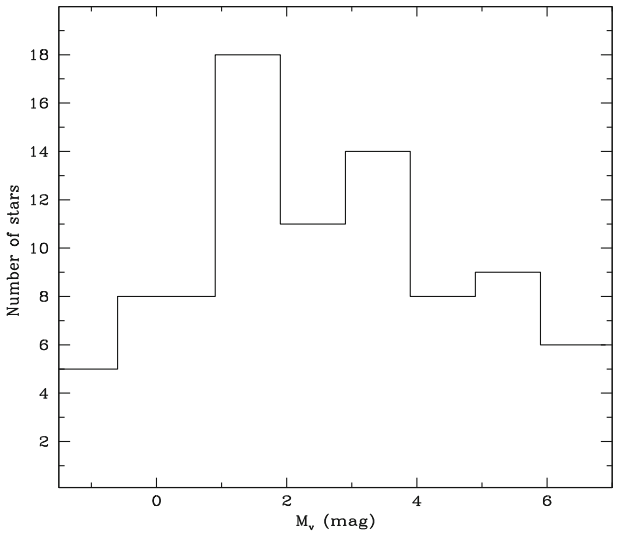

Figure 8. The brightness distribution, i.e., luminosity function of the open cluster NGC 1513.

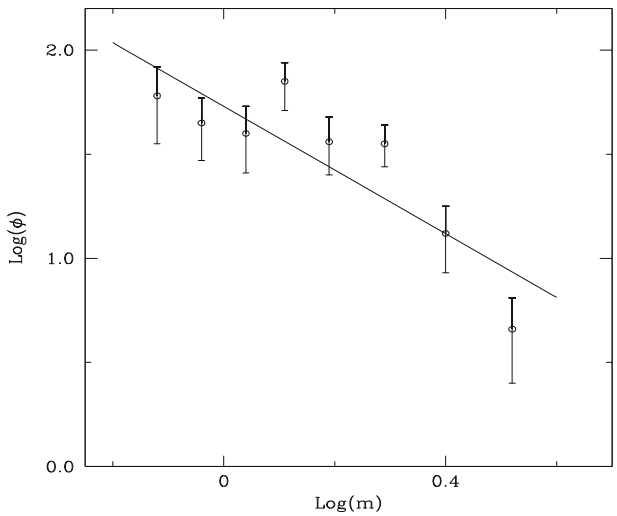

Figure 9. The mass function of the open cluster NGC 1513 was derived using mass luminosity relation given by Girardi *et al.* (2000) models.

bin dM with central mass M and x is the slope of the MF. The MF slope derived in this analysis is $x = 0.53 \pm 0.37$. The present estimate is very close to the value of 0.54 ± 0.36, derived by Maciejewski & Niedzielski (2007). However, Our derived value is lower than the Salpeter (1955) value of 1.35 derived for field stars in the Solar neighborhood.

6. Galactic globular cluster NGC 4147

The globular star cluster NGC 4147 ($\alpha_{2000} = 12^h10^m 6.2^s$; $\delta_{2000} = +18°32'31''$; $l = 253°$, $b = +77°$) is a halo object (Harris 2010). It is located near the boundary between the third and fourth Galactic quadrants, and not far from the north Galactic pole. The foreground reddening, $E(B - V) = 0.02$ mag, is very small. This globular cluster is located at a distance of 17.3 kpc and 19.1 kpc from the Sun and the Galactic center, respectively. This indicates that the cluster is a member of the halo rather than disk population. The cluster metallicity ($[Fe/H] = -1.83$) listed in Harris (2010) catalog is very low.

6.1 *Optical observations of NGC 4147*

The CCD images of the NGC 4147 were obtained with the 3.6-m DOT in standard Bessel B and R filters on 24 March 2017 using the CCD imager described above in Section 2.1. Several images of 600 s were taken in each B and R pass bands. Furthermore, observations were taken in 4×4 pixel binning mode and all images in a filter were stacked together to improve the signal-to-noise ratio (S/N) for relatively fainter stars. The mean FWHM of the stars is 3.5 pixels (0.35 arc-sec). The bias and flat frames were acquired during the observations. These calibration frames were used to clean the science frames using the standard IRAF. The DAOPHOT/ALLSTAR (Stetson 1987, 1992) package was used to derive instrumental magnitudes. Quadratically varying PSFs were used to derive instrumental magnitudes. They were converted to the standard system using 375 Stetson standard stars present in the field of NGC 4147[2]. The B and R magnitudes of the stars obtained in this way are listed in Table 4 along with their pixel, RA and Dec coordinates. The mean error is $\sim$0.1 mag at 24th mag. The format of the data is shown in Table 4 while the entire data table consisting of 1825 stars is available online. The data table can also be obtained from the corresponding author.

6.2 *The color-magnitude diagram of NGC 4147*

The B, $(B - R)$ CMD of NGC 4147 is shown in Figure 10. All the stars observed in B and R filter having an error better than 0.1 mag are shown in the figure. The main-sequence, giant branch and horizontal branch are visible in the CMD. The main sequence extends up to $\sim$24 mag towards the fainter end.

[2]https://www.canfar.net/storage/vault/list/STETSON/Standards.

Table 4. This is a sample table of the catalog for the Galactic globular cluster NGC 4147.

ID	X (pixel)	Y (pixel)	RA (J2000)	Dec (J2000)	B (mag)	eB (mag)	R (mag)	eR (mag)	MP
1	670.600	8.431	12:10:02.27	18:35:43.8	20.072	0.005	18.256	0.006	0
2	650.973	15.857	12:10:02.80	18:35:40.9	21.529	0.018	20.775	0.021	0
3	640.832	47.934	12:10:03.07	18:35:28.6	20.573	0.008	19.873	0.014	0
4	943.470	51.257	12:09:54.93	18:35:28.2	20.902	0.012	20.232	0.016	0
5	763.679	65.565	12:09:59.76	18:35:22.2	21.158	0.014	20.421	0.015	0
–	–	–	–	–	–	–	–	–	–
–	–	–	–	–	–	–	–	–	–

Full table is available electronically. The (X, Y) pixel positions, RA, Dec sky coordinates and the B and R CCD magnitudes with corresponding DAOPHOT errors are listed in columns 2 to 9 while the GAIA EDR3 proper motion MP is provided in the last column. For most of the stars fainter than $V = 21$ mag, MP could not be estimated due to lack of proper motion data.

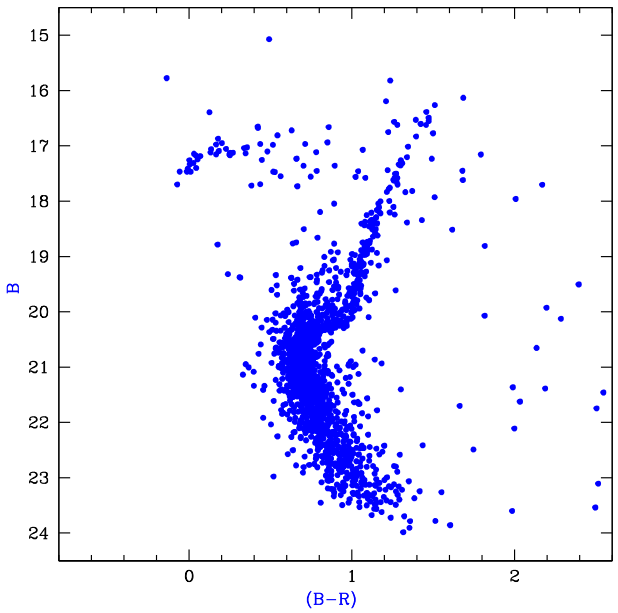

Figure 10. The B, $(B-R)$ CMD of the globular cluster NGC 4147 using the data obtained with the 4K×4K CCD imager mounted at the axial port of the 3.6-m DOT on 24 March 2017.

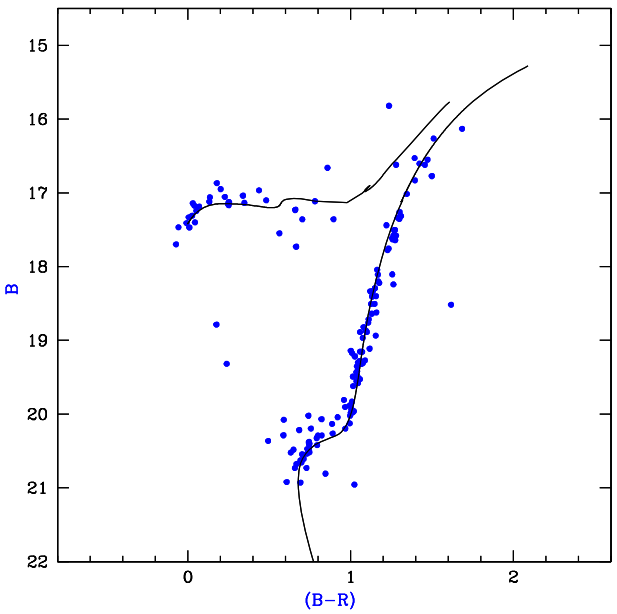

Figure 11. The B, $(B-R)$ CMD of the globular cluster NGC 4147 using the stars having MP $\geq 50\%$. The solid line shown in the diagram is a 14 Gyr isochrone taken from BaSTI (Hidalgo *et al.* 2018) for $Z = 0.0003$.

In order to estimate age and distance of the cluster, we identified GAIA EDR3 proper motion cluster members using procedure described above in Section 3.2. The $(\mu_{xc}, \mu_{yc}) = (-1.7, -2.1)$ mas yr^{-1} have been estimated from stars having proper motion error ≤ 1 mas yr^{-1}. The proper motion dispersion has been calculated as 0.03 mas yr^{-1} by considering a distance of 18.2 kpc derived in this section, and radial velocity dispersion 2.84 km s^{-1} taken from Baurgardt & Hilket (2018). For field stars, we have $(\mu_{xf}, \mu_{yf}) = (-1.9, -2.2)$ mas yr^{-1} and $(\sigma_{xf}, \sigma_{yf}) = (1.6, 1.7)$ mas yr^{-1}.

The age and distance of the cluster are estimated by the visual fitting of the theoretical stellar evolutionary isochrone provided by Hidalgo *et al.* (2018) to the CMD. The B, $(B-R)$ CMD of 236 stars having MP $\geq 50\%$ is plotted in Figure 11. We could, therefore, plot only stars with $V \leq 21$ mag. We superimposed the isochrone of age 14 Gyr with metallicity $Z = 0.0003$ in Figure 11. The fitting of isochrone is done with distance modulus $(m-M) = 16.35$ mag and $E(B-R) = 0.02$ mag. The estimated distance modulus provides a heliocentric distance of the cluster as 18.2 kpc which is identical to the value of 18.2 kpc derived by Baumgardt & Hilket (2018).

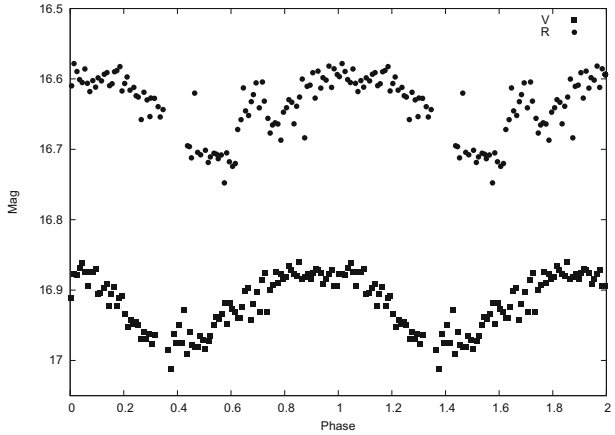

Figure 12. *V* and *R* band light-curves of the star number *V*24 in Table 2 by Lata *et al.* (2019). It is numbered as HB24 in Table 4 of Kumar *et al.* (2021a,b,c,d).

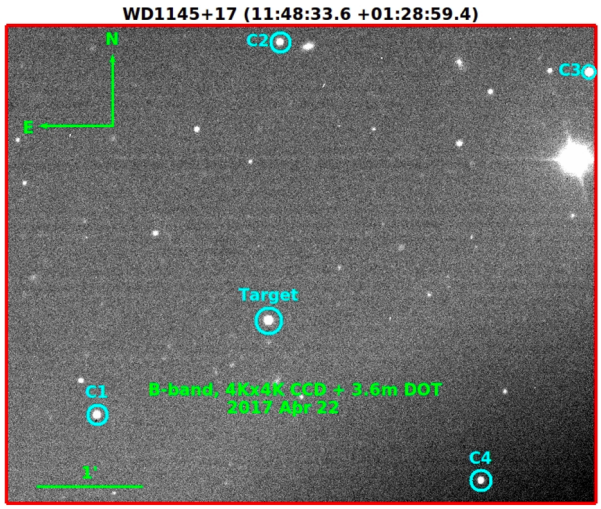

Figure 13. Finding chart of the WD 1145+017 field showing the four comparison stars and the White Dwarf candidate as observed with the 3.6-m DOT and 4K×4K imager in *B*-band.

Optical identification of AstroSat discovered sources was one of the prime goals of the 3.6-m DOT and the 4K×4K CCD imager (Sagar 2018; Pandey *et al.* 2018). Recently, Kumar *et al.* (2021a,b,c,d) identified several AstroSat-UVIT sources in the field of NGC 4147. These objects are located in different stages of stellar evolution in the UV-optical CMDs showing properties of blue horizontal branch stars, blue straggler stars and variable stars. While Lata *et al.* (2019) have discovered several different types of variables within the core region of the NGC 4147 using optical observations taken with the 4K×4K CCD imager mounted on the 3.6-m DOT. However, only one object, located at RA = 182.527222 and Dec = 18.55061 (J2000), is common between these two studies. This far-UV identification of an optical source within a half-light radius of the NGC 4147 shows properties of a RR Lyrae type of variables/eclipsing binary. The optical light curve of this common object is also shown in Figure 12.

7. Optical monitoring of white dwarf WD 1145+017

The transiting behavior of the dusty debris clouds orbiting around white dwarf WD 1145+017 was discovered by Kepler *K*2 mission (Vanderburg & Rappaport 2018). Recent observations of WD 1145+017 are recently studied by Xu *et al.* (2018) and references therein. These dust clouds reveal themselves through deep, broad and evolving transits in the star's light curves. Such observations have shown transits with multiple periods ranging from 4.5 to 4.9 h and transit duration ranging from $\sim$3 min to as long as an hour (Xu *et al.* 2018; Rappaport *et al.* 2018 and references therein). Here, we report CCD optical *B* pass band photometric observations of WD 1145+017 taken with the 3.6-m DOT on the night of 22–23 April 2017. Technical details of the CCD imager used by us are given in Section 2.1. The data was collected in the 4×4 binning modes with 1-MHz readout frequency (Pandey *et al.* 2018). During 5.5 h of our observations, a total of 210 continuous frames were acquired. Their exposure times ranged from 70 to 80 s. Along with target field, bias, dark and twilight flat-field frames were also collected for calibration purposes. The basic image processing of the images was performed using IRAF.

The finding chart of the white dwarf is displayed in Figure 13. In order to create differential light curves, we used 4 comparison stars identified as C1, C2, C3 and C4 in the Figure 13. All comparison stars are ≤ 1 mag fainter than the white dwarf. The FWHM of stellar images during our 5.5 h of observations varied between 0.″8 and 1.″1. The instrumental magnitudes of the stars were obtained using the DAOPHOT package (Stetson 1987). In Figure 14, differential magnitudes of WD 1145+017 with respect to all comparison stars are plotted against time of observations in the upper 4 panels and shown with blue color while differential magnitudes of comparison stars C2, C3 and C4 with respect to C1 are plotted against time of observations in lower 3 panels and shown with red

color. The DAOPHOT (or signal-to-noise) errors in our observations are $\sim$0.015 mag. Statistically significant variabilities are not observed in the comparison stars during the entire period of our observations. While differential light curves of WD 1145+017 exhibit three dips. They are similar with respect to all 4 comparison stars. The shape and depth of first and last dips are similar and separated by $\sim$4.6 h. Since the transit period of the objects revolving around the white dwarf ranges from 4.5 to 4.9 h, both the first and last dips of $\sim$20 min duration correspond to the same orbiting body. It looks similar to dip A1 as reported by Xu *et al.* (2018) in Figure 1 discussing about their optical observations. The duration of the second dip is $\sim$80 min and the light curve is quite complex in comparison to the other two dips. Light curves with sharp decline and increase with shorter duration may indicate that orbiting object is solid and small in size while complex and longer duration light curve could be due to transit of dusty and larger sized body. A deeper analysis and modeling of these observations are in progress.

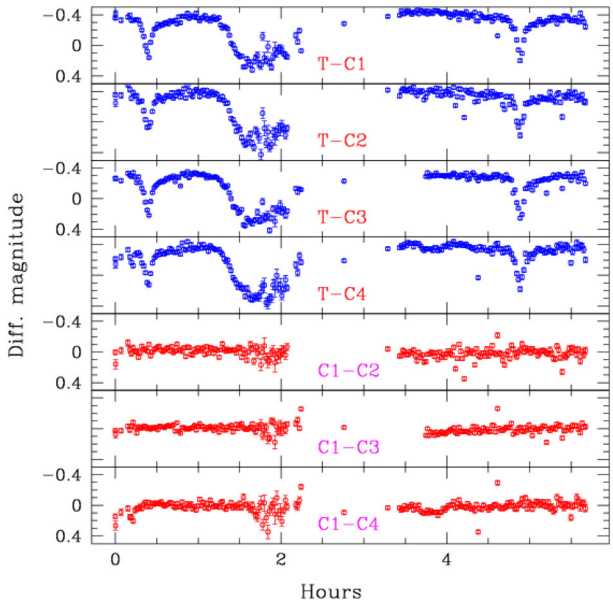

Figure 14. Differential light curve of WD 1145+017 with respect to all comparison stars are plotted in upper 4 panels (shown in blue color) while differential magnitude of comparison stars C2, C3 and C4 with respect to star C1 are plotted against time of observations in lower 3 panels (red color). Beginning of our $\sim$5.5 h long observations corresponds to Julian date 2457866.109, i.e., 14:38:01 Universal time on 22 April 2017.

8. Deep high-resolution images of Sh 2-61 in *K* band using the TIRCAM2 on 3.6-m DOT

Deep *K*-band (2.19 μm) photometric observations of the Sharpless region 'Sh 2-61'[3] (α_{J2000} : $18^h33^m21^s$, $\delta_{J2000} = -04°58'02''$) were taken during the night of 23 May 2017 using TIRCAM2 (Naik *et al.* 2012; Baug *et al.* 2018) mounted at the Cassegrain main port of the 3.6-m DOT. The weather conditions in these nights were good with a relative humidity of <60% and the FWHM of the stellar images were $\sim$0.″5. The field of view (FOV) of the TIRCAM2 is $\sim$86.″5 × 86.″5 square with a plate scale of 0.″167. We took 101 frames

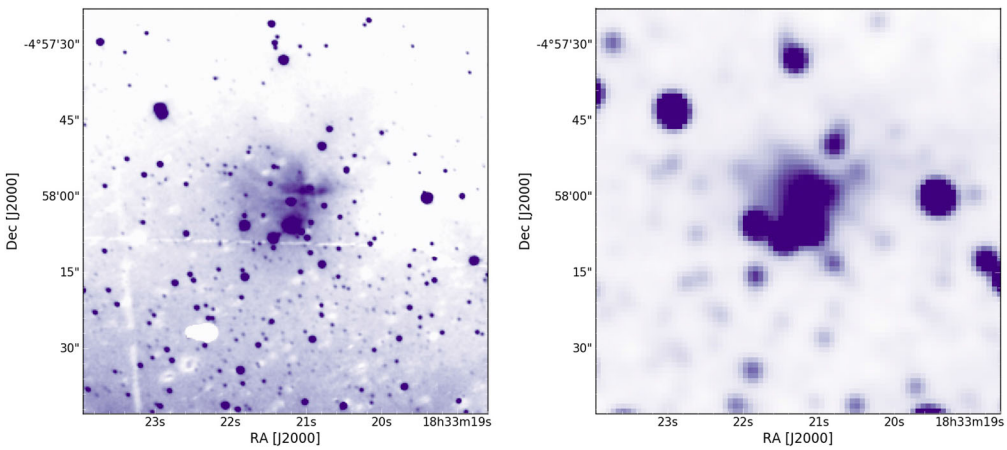

Figure 15. *K*-band image of Sh 2-61 region using the TIRCAM2 (left panel) and 2MASS (right panel) for a 80 × 80 arcsec square FOV.

[3] http://galaxymap.org/cat/view/sharpless/61.

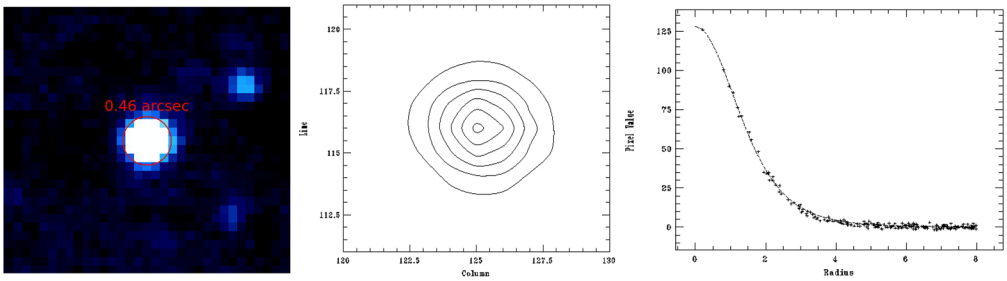

Figure 16. *K*-band image of a stellar profile (left panel), intensity contours (middle panel), and radial profile (right panel) using the TIRCAM2 on 3.6-m DOT. The image profile is a very sharp and is almost circular (ellipticity = 0.02). A circle of radius 0.46 arc-sec (FWHM of PSF) is also shown in the left panel.

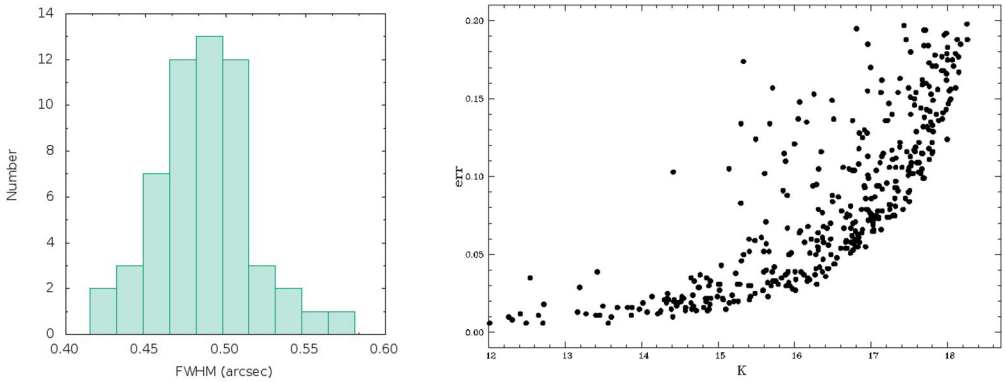

Figure 17. Left panel: Distribution of the FWHM of the stellar sources in the TIRCAM2 field of view. The FWHM varies from 0.43 to 0.58 arc-sec with a peak around $\sim$0.5 arc-sec. Right panel: DAOPHOT error as a function of *K*-band magnitude. The source of $K \sim 18.2$ mag is detected in $\sim$17 min exposure with error $\sim$0.2 mag (S/N $\sim$ 5).

in a dithered pattern around the central region of Sh 2-61 with an exposure time of 10 s, i.e., the total exposure time was $\sim$17 min. Dark and sky flats were also taken during the observations. Sky frame was generated from the median of the dithered frames.

The basic image processing such as dark/sky subtraction and flat-fielding was done using tasks available within IRAF. The final image was generated by aligning and combining the sky subtracted frames and is shown in the left panel of Figure 15. For comparison, we have also shown the 2MASS image of a similar FOV. Using TIRCAM2 we can resolve far more stars than 2MASS and observe dust and gas emission near the central region of Sh 2-61. In Figure 16, we have demonstrated the sharp image quality of the TIRCAM2 data as evident from the low ellipticity ($\sim$0.02) and FHWM ($\sim 0.''46$) of a stellar image. In the left panel of Figure 17, we have shown the distribution of FWHM of the stellar profile in the final image. The distribution also points towards a good quality image from TIRCAM2 as the FWHM varies from $0.''43$ to $0.''58$ with median $\sim 0.''5$. The instrumental magnitudes from the final image were obtained using the DAOPHOT package. As the region is crowded, we carried out PSF photometry to get the magnitudes of the stars. Astrometry of the stars was done using the Graphical Astronomy and Image Analysis Tool[4] with an rms noise of the order of $\sim 0''28$. The calibration of the photometry to the standard system was done using the offset calculated from the 2MASS data. The typical DAOPHOT errors as a function of corresponding standard magnitudes are shown in the right panel of Figure 17. In total, 405 stars were identified in the central region of the Sh 2-61 with error <0.2 mag with detection up to $K \sim 18.2$ mag. 2MASS has detected only 67 stars in the same FOV. All these demonstrate the deep and high-resolution imaging capability of TIRCAM2 on 3.6-m DOT in NIR bands.

9. Summary and conclusions

Optical observations of an open cluster NGC 1513, a galactic globular cluster NGC 4147 and a white dwarf WD 1145+07 and *K*-band imaging of a star-forming

[4] http://star-www.dur.ac.uk/$\sim$pdraper/gaia/gaia.html.

region Sh 2-61 with 3.6-m DOT are presented here. These observations were taken between November 2016 and May 2017. The main findings of the present analysis are as follows:

- The GAIA EDR3 proper motion data are used to identify 106 likely members in the open star cluster NGC 1513 having mean proper as $\mu_\alpha \cos\delta = 1.29 \pm 0.02$ and $\mu_\delta = -3.74 \pm 0.02$ mas yr^{-1}.
- Using the two-color diagram, we estimated reddening $E(B-V)$ as 0.65 ± 0.03 mag to the NGC 1513. Distance to the cluster is determined as 1.33 ± 0.10 kpc while age is estimated as 225 ± 25 Myr by comparing the cluster's sequence with the theoretical isochrones of solar metallicity given by Girardi *et al.* (2000).
- Based on the B, $(B-R)$ CMD of the GAIA EDR3 proper motion members, We determined the distance and age of the galactic globular cluster NGC 4147 as 18.2 kpc and 14 Gyr, respectively.
- The values of FWHM estimated from images of stellar sources are expected to be slightly more than the value of atmospheric seeing prevailing at the epoch of observations (Sagar *et al.* 2020). Atmospheric seeing is λ dependent and varies as $\lambda^{-0.2}$. Observations reported here and earlier by Sagar *et al.* (2019a,b, 2020) and recently by Panwar *et al.* (2022) show that at Devasthal, for a good fraction of observing time, optical to NIR sky images with sub-arc-sec resolution can be obtained with the 3.6-m DOT. These good sky conditions enable deep imaging of stars with detection of $B = 24.5 \pm 0.2$, $R = 24.6 \pm 0.12$ and $V = 25.2 \pm 0.2$ mag stars in exposure time of 1200, 4320 and 3600 s, respectively. The NIR observations taken with TIRCAM2 show that stars up to $J = 20 \pm 0.1$, $H = 18.8 \pm 0.1$ and $K = 18.2 \pm 0.1$ mag can be detected in effective exposure times of 500, 550 and 1000 s, respectively.
- The modern active optics 3.6-m DOT observing facilities have started providing good quality of optical and NIR observations for a number of front lines Galactic and extragalactic astrophysical research problems including optical follow up of γ-ray, X-ray, UV and radio sources observed with facilities like GMRT and AstroSat, etc., and optical transients objects like SN and afterglows of γ-ray bursts and a gravitational wave, etc. The telescope has therefore started contributing significantly to the growth of our understanding of Astrophysical jets.

Acknowledgments

This manuscript is based on an invited talk delivered during an international workshop Astrophysical Jets and Observational Facilities: National Perspective held by ARIES from 5–9 April 2021. One of us (Ram Sagar) thanks to the National Academy of Sciences, India (NASI), Prayagraj, for the award of a NASI Honorary Scientist position; the Alexander von Humboldt Foundation, Germany, for the award of Group linkage long-term research program; and the Director, IIA, for hosting and providing infrastructural support during this work. SBP acknowledges financial support received from the BRICS grant DST/IMRCD/BRICS/PilotCall1/ProFCheap/2017(G). SJ thanks Nand Kumar and Amit Kumar for their help in data analysis and preparing the figures. The 3.6-m Devasthal Optical Telescope (DOT) is a National Facility run and managed by Aryabhatta Research Institute of Observational Sciences (ARIES), an autonomous Institute under the Department of Science and Technology, Government of India. This research has made use of data obtained from the High Energy Astrophysics Science Archive Research Center (HEASARC) and the Leicester Database and Archive Service (LEDAS), provided by NASA's Goddard Space Flight Center and the Department of Physics and Astronomy, Leicester University, UK, respectively. This work has made use of data from the European Space Agency (ESA) mission GAIA processed by Gaia Data processing and Analysis Consortium (DPAC), (https://www.cosmos.esa.int/web/gaia/dpac/consortium). It is worthy to mention that, this work has also used WEBDA.

References

Balaguer-Nunez L., Tian K. P., Zhao J. L. 1998, A&AS, 133, 387
Baumgardt H., Hilket M. 2018, MNRAS, 478, 1520
Barkhatova K. A., Dryakhlushina L. I. 1960, SvA, 4, 313
Baug T., *et al.* 2018, J. Astron. Instrum., 7, 1850003
Bronnikova N. M. 1958, TrPul, 72, 77
Cantat-Gaudin T., Jordi C., Vallenari A., *et al.* 2018, A&A, 618, 93
del Rio G., Huestamendia G. 1988, A&AS, 73, 425

Fabricius C., Luri X., Arenou C., *et al.* 2021, A&A, 649, A5
Frolov V. N., Jilinski E. G., Ananjevskaja J. K., Poljakov E. V., Bronnikova N. M., Gorshanov D. L. I. 2002, A&A, 396, 125
Girad T. M., Grundy W. M., Lopez C. E., van Altena W. F. 1989, AJ, 98, 227
Gaia Collaboration *et al.* 2018, A&A, 616, A1
Girardi L., Bressan A., Bertelli G., Chiosi C. 2000. A&AS, 141, 371
Gupta R., *et al.* 2021a, MNRAS, 505, 4086
Gupta R., *et al.* 2021b, 2022, JApA, 43, (accepted)
Harris W. E. 2010, arXiv:10123224v1 [Astro-ph]
Hidalgo S. L., *et al.* 2018, ApJ, 856, Art. 125, https://doi.org/10.3847/1538-4357/aab158
Kumar B., *et al.* 2018, BSRSL, 87, 29
Kumar A., *et al.* 2021a, MNRAS, 502, 1678
Kumar A., Pandey S. B., Gupta R., *et al.* 2021b, Revista Mexicana de Astronomia y Astrofisica Conference Series, 53, 127, https://doi.org/10.22201/ia.14052059p.2021.53.25
Kumar A., Pandey S. B., Singh A., *et al.* 2021c, arXiv:2111.13018
Kumar R., Pradhan A. C., Parthasarthi M., *et al.* 2021d, JApA, 42, https://doi.org/10.1007/s12036-020-09687-y
Landolt A. U. 1992, AJ, 104, 340
Lata S., *et al.* 2019, AJ, 158, 158, 51, https://doi.org/10.3847/1538-3881/ab22a6
Ojha D. K., *et al.* 2018, BSRSL, 87, 58
Omar A., *et al.* 2017, Curr. Sci., 113, 682, https://doi.org/10.18520/cs/v113/i04/682-685
Omar A., *et al.* 2019a, Curr. Sci., 116, 1472, https://doi.org/10.18520/cs/v116/i9/1472-1478
Omar A., *et al.* 2019b, JApA, 40, https://doi.org/10.1007/s12036-019-9583-4
Omar A., *et al.* 2019c, BSRSL, 88, 31
Maciejewski G., Niedzielski A. 2007, A&A, 467, 1065
Naik M. B. *et al.* 2012, BASI, 40, 531
Pandey S. B. 2016, Revista Mexicana de Astrono-mia y Astrofisica Conference Series, Vol. 48, RevistaMexicana de Astronomia y Astrofisica Conference Series, p 83
Pandey S. B., *et al.* 2018, BSRSL, 87, 42
Pandey S. B., *et al.* 2021, MNRAS, 507, 1229
Panwar N., Kumar A., Pandey S. B. 2022, JoAA, 43, 7, https://doi.org/10.1007/s12036-021-09785-5
Rappaport, *et al.* 2018, MNRAS, 474, 933
Sagar R. 2018, BSRSL, 87, 391
Sagar R., *et al.* 2000, A&AS, 144, 349
Sagar R., *et al.* 2019a, Curr. Sci., 117, 365, https://doi.org/10.18520/cs/v117/i3/365-381
Sagar R., *et al.* 2019b, BSRSL, 88, 70
Sagar R., Kumar B., Sharma S. 2020, JApA, 42, https://doi.org/10.1007/s12036-020-09652-9
Salpeter E. E. 1955, ApJ, 121, 161
Schmidt-Kaler T. 1982 in Scaitersk, Voigt H. H., eds, Landolt/Bornstein, Numerical Data and Functional Relationship in Science and Technology, New series, Group VI, Vol. 2b, Springer-Verlag, Berlin, p 14
Stalin C. S., *et al.* 2001, BASI, 29, 39
Stetson P. B. 1987, PASP, 99, 191
Stetson P. B. 1992, in Warral D. M., Biemesderfer C., Barnes J., eds ASP, Conf. Ser. Vol. 25, Astronomical data analysis software and system I. Astron. Soc. Pac., San Francisco, p 297
Trumpler R. J. 1930, Lick Obs. Bull., 14, 154
Vanderburg A., Rappaport S. 2018, Transiting Disintegrating Planetary Debris around WD 1145+017 (Springer-Verlag: Berlin)
Xu S., *et al.* 2018, MNRAS, 474, 4795
Yadav R. K. S., Bedin L. R., Piotto G., *et al.* 2008, A&A, 484, 609
Yadav R. K. S., Sariya D., Sagar R. 2013, MNRAS, 430, 3350